

**Predicting the movements of permanently installed  
electrodes on an active landslide using time-lapse  
geoelectrical resistivity data only**

(Abbreviated title: Electrode movements from resistivity data)

Paul B. Wilkinson\*, Jonathan E. Chambers, Philip I. Meldrum, David A. Gunn,  
Richard D. Ogilvy, and Oliver Kuras

Accepted 2010 August 3. Received 2010 June 17; in original form 2010 January 20

British Geological Survey, Kingsley Dunham Centre, Keyworth, Nottingham, NG12  
5GG, UK

\*Corresponding Author. Fax: +44 115 936 3261. Email: [pbw@bgs.ac.uk](mailto:pbw@bgs.ac.uk)

Published in *Geophysical Journal International* (Royal Astronomical Society / Blackwell Publishing). The definitive version is available at [www.blackwell-synergy.com](http://www.blackwell-synergy.com)

*Geophysical Journal International* (2010) **183**, 543-556  
<http://onlinelibrary.wiley.com/doi/10.1111/j.1365-246X.2010.04760.x/pdf>

## Abstract

If electrodes move during geoelectrical resistivity monitoring and their new positions are not incorporated in the inversion, then the resulting tomographic images exhibit artefacts that can obscure genuine time-lapse resistivity changes in the subsurface. The effects of electrode movements on time-lapse resistivity tomography are investigated using a simple analytical model and real data. The correspondence between the model and the data is sufficiently good to be able to predict the effects of electrode movements with reasonable accuracy. For the linear electrode arrays and 2D inversions under consideration, the data are much more sensitive to longitudinal than transverse or vertical movements. Consequently the model can be used to invert the longitudinal offsets of the electrodes from their known baseline positions using only the time-lapse ratios of the apparent resistivity data. The example datasets are taken from a permanently installed electrode array on an active lobe of a landslide. Using two sets with different levels of noise and subsurface resistivity changes, it is found that the electrode positions can be recovered to an accuracy of 4 % of the baseline electrode spacing. This is sufficient to correct the artefacts in the resistivity images, and provides for the possibility of monitoring the movement of the landslide and its internal hydraulic processes simultaneously using electrical resistivity tomography only.

**Keywords:** Inverse theory; Tomography; Time series analysis; Hydrogeophysics.

## Introduction

Electrical Resistivity Tomography (ERT) is the most widely applied geophysical technique used to investigate landslides (Jongmans & Garambois 2007). It produces 2D or 3D images of the spatial subsurface resistivity structure of the landslide. Due to the strong dependence of resistivity on saturation, fracturing, clay content and weathering, it is often used to image failure surfaces (Perrone *et al.* 2004; Lapenna *et al.* 2005; Lebourg *et al.* 2005; Naudet *et al.* 2008; Sass *et al.* 2008). Repeated time-lapse resistivity surveys have been carried out to assess the effects of saturation in landslide-prone areas (Suzuki & Higashi 2001; Friedel *et al.* 2006; Jomard *et al.* 2007), and conceptual models have been developed to relate time-lapse resistivity changes to slope failure (Piegari *et al.* 2009). Recently several researchers have highlighted the possibility of continuously monitoring landslide bodies using automated resistivity tomography systems with permanently installed electrode networks (Lapenna *et al.* 2005; Meric *et al.* 2005). Prototype systems have now been deployed to monitor a number of active landslides using this approach (Supper *et al.* 2008; Chambers *et al.* 2009; Lebourg *et al.* 2009). By providing information on subsurface hydrogeological changes with high spatial and temporal resolution, these systems aim to reveal the hydraulic precursors to landslide movement.

Although time-lapse ERT is particularly well-suited to monitoring hydraulic processes (Kuras *et al.* 2009), the measured potentials do not depend solely on the resistivity, but also on the positions of the electrodes. In geoelectrical imaging these are usually assumed to be known and accurate. Recently several groups have quantified the systematic errors that are caused in resistivity data by errors in the positions of electrodes (Zhou & Dahlin 2003; Oldenborger *et al.* 2005; Wilkinson *et al.* 2008). Where permanently installed electrodes have been used for time-lapse

monitoring, it has typically been assumed that the electrode locations are static. But this is clearly not the case if they are installed on an active landslide. To our knowledge, no-one has previously addressed the artefacts caused by mobile electrodes in time-lapse geoelectrical imaging (although Supper *et al.* (2008) qualitatively identified anomalous changes in potential which they attributed to landslide movement, and Zhou & Dahlin (2003) and Oldenborger *et al.* (2005) showed similar artefacts caused by a static misplaced electrode). However this problem has been recognised for several years in the related discipline of medical Electrical Impedance Tomography (EIT), since posture changes and breathing cause electrodes to move during imaging (Zhang & Patterson 2005). Research is ongoing in EIT imaging to invert the time-lapse impedance data to recover the unknown time-varying electrode positions simultaneously with the impedance distribution (Blott *et al.* 1998; Soleimani *et al.* 2006; Gómez-Laberge & Alder 2008; Dai *et al.* 2008; Li *et al.* 2008). Since medical EIT usually involves weak impedance contrasts, these approaches use one-step linearised inversions that are less well suited to imaging the much stronger resistivity contrasts that occur in geoelectrical surveys.

In this paper, we develop a new approach to recover the movements of permanently installed electrodes that are part of an array being used to monitor a landslide. We briefly describe the landslide research site and the Automated time-Lapse ERT (ALERT) monitoring system, and we discuss the baseline image of the resistivity structure of the landslide body. Significant movements of the electrodes occurred due to landslide activity in the winter months after the baseline imaging. We show that, if the electrode positions are not corrected, these movements cause appreciable artefacts in later resistivity images. Although the effects on the data of resistivity changes and electrode movements are non-linear and coupled, by making

reasonable assumptions we propose a method that allows the electrode positions to be determined independently. We discuss the validity these assumptions and identify situations where more sophisticated techniques might be required. Finally, by using real time-lapse data from the landslide research site, we demonstrate that we can identify and correct the electrode positions before inverting for the resistivity distribution. This removes the image artefacts and improves the fit between the model and the data without having to repeatedly visit the site to resurvey the electrode locations.

## Research Site

The data sets in this paper were acquired from an active landslide site 12 km to the west of Malton, North Yorkshire, UK. The site is being monitored with an ALERT system (Kuras *et al.* 2009; Ogilvy *et al.* 2009) to study the hydraulics of landslide processes in near real-time. The system is battery powered with wind and solar recharging and operates fully autonomously with no need for user intervention. The ALERT instrument uses wireless telemetry (in this case GPRS) to communicate with an office based PC that runs control software and a database management system. The control software is used to schedule data acquisition, while the database management system automatically stores, processes and inverts the remotely streamed resistivity data.

The landslide research site is located on a south facing valley side with a slope of approximately 12°. The bedrock geology, from the base to top of slope, comprises the Lias Group Redcar Mudstone Formation (RMF), Staithes Sandstone and Cleveland Ironstone Formation (SSF), and Whitby Mudstone Formation (WMF), which are overlain at the top of the hill by the Dogger Sandstone Formation (DF) (see Figure 1). The bedrock is relatively flat lying with a gentle dip of a few degrees to the

north (British Geological Survey 1983). Slope failure at the site is occurring in the weathered WMF, which is highly prone to landsliding. The landslide is a very slow to slow moving composite multiple earth slide - earth flow, according to the classification scheme proposed by Cruden and Varnes (1996). The upper sections to the north are characterised by rotational slides with multiple minor scarps and cracking within the WMF, which evolve into heavily fissured earth flows that form discrete lobes of slipped material overriding the SSF bedrock to the south. Borehole logs from the western lobe (Figure 1) indicate a maximum thickness of slipped material within the earthflows of approximately 5 m.

The data were collected from one of five permanently installed parallel linear electrode arrays running from the base to the top of the hill (dark and light blue lines, Figure 1). These formed an initially regular rectangular grid of 38 m  $\times$  147.25 m. Each linear array comprised 32 electrodes initially spaced at 4.75 m (Chambers *et al.* 2009), and the inter-line spacing was 9.5 m. The array that was selected for this study ran along one of the active lobes of the landslide (dark blue line, Figure 1). Data were acquired from the arrays on a daily basis using a dipole-dipole measurement scheme with dipole lengths of  $a = 4.75, 9.5, 14.25$  and 19 m, and dipole separations  $na$ , where  $n = 1 - 8$ . Each of the 516 measurements was made twice in reciprocal configurations (Parasnis 1988), with the mean of the two measurements being taken as the apparent resistivity for that particular configuration. The difference between the measurements was used to calculate the standard error in the mean for each configuration, which we refer to as its reciprocal error. This was used to estimate the levels of the random error in the data and to weight the data accordingly in the resistivity inversions. The distributions of reciprocal errors in the data sets are given in Table 1. The greater reciprocal errors in August 2009 compared to either March 2008 or March 2009 are

due to the increased contact resistances typically encountered in the summer months caused by drying of the ground in the vicinity of the electrodes. The mean, minimum and maximum contact resistances in August 2009 were 535  $\Omega$ , 175  $\Omega$ , and 3415  $\Omega$  respectively. The corresponding values for March 2009 were 165  $\Omega$ , 115  $\Omega$ , and 365  $\Omega$ . Nevertheless, even in August the data quality is still excellent, with over 90 % of the data having reciprocal errors <1 %.

**Table 1.** Reciprocal error distributions

Reciprocal error level	Fraction of data set below reciprocal error level		
	March 2008	March 2009	August 2009
0.10 %	75 %	72 %	52 %
0.25 %	92 %	91 %	71 %
0.50 %	98 %	98 %	84 %
1.0 %	99 %	99 %	92 %
5.0 %	100 %	100 %	97 %

The ALERT system and electrodes were installed in March 2008 at which time the electrode positions were surveyed using the Leica SmartRover, a real-time kinematic GPS receiver with centimetric accuracy. The baseline dataset used in this study was acquired shortly after installation in the same month. The inverted resistivity image of these data is shown in Figure 2 and the raw data are shown as a pseudosection in Figure 3a. The data were inverted with the Res2DInv software using a finite-element method to permit the inclusion of topography, a complete Gauss–Newton solver, and  $L_2$  model smoothness and data discrepancy constraints (Loke *et al.* 2003). Convergence was achieved after 5 iterations with an extremely good fit between the measured and inverted data, as indicated by an RMS error of 1.02 %. The image exhibits resistivity variations consistent with the expected stratigraphic sequence, with the mudstone formations significantly more conductive than the SSF. There is clear evidence of slipped conductive WMF material overlying the SSF between distances of 60 m and 80 m. Within the WMF, the higher surface resistivities

in the vicinity of the main scarp are most likely due to increased localised fracturing. The position of the WMF / SSF boundary was inferred from the resistivity image, while the SSF / RMF boundary has been positioned to match the log of an auger hole at  $x = -6$  m. In recent years, the active lobes of the landslide have been observed to move by many tens of centimetres per annum. Movement typically occurs in the winter months of January and February when the slope is at its wettest. During this period water can be observed accumulating in the basins caused by rotational slips near the top of the slope, and can be seen emerging from the front of the lobes. Drainage from the site also occurs along a spring line at the base of the SSF, where groundwater appears to be running off the surface of the less permeable underlying RMF. Recently installed piezometers have revealed elevated pore pressures at the failure planes within the slipped WMF and at the interface between the slipped WMF material and the underlying SSF, as indicated by head increases within the lobes of almost 2 m during the winter as compared to the summer months.

In this paper, we consider two subsequent resistivity data sets, both acquired after the winter 2008/2009 period of movement had finished. The first of these sets was measured in March 2009 under similar saturation and temperature conditions to the baseline set of March 2008. The second was from August 2009, at which time the electrode positions were resurveyed. The raw data for March 2009 are shown as a resistivity pseudosection in Figure 3b and as a normalised pseudosection (i.e. divided by the baseline data) in Figure 3c. Similarly the August 2009 data are shown in Figure 3d and Figure 3e. Inverted images of these data are shown in Figure 4a and Figure 4c respectively. The images and pseudosections were produced under the assumption that the electrodes had not moved from their March 2008 positions. Compared to the baseline set, there is noticeable new structure in the regions of the images highlighted

by the dashed ellipses. This is revealed more clearly in Figure 4b and Figure 4d, which show the March and August 2009 images normalised to the baseline image. It is also worth noting that the RMS misfit errors (1.45 % and 1.46 % respectively) are somewhat larger than that of the baseline set. These changes are also clearly visible in the resistivity and normalised pseudosections in Figure 3, appearing as linear anomalies radiating from the region centred on electrode 9. The changes seemed unlikely to be due to the sudden appearance of genuine localised resistivity structures, since no similar anomalies were present in the baseline image or pseudosection. Therefore we concluded that they were most likely to be artefacts caused by the use of incorrect electrode positions.

## Effects of electrode movement

To investigate further, we examined the effects on the measured apparent resistivities caused by changing the positions of the electrodes in linear dipole-dipole configurations. The electrode movements between March 2008 and August 2009 are shown in Figure 5 as longitudinal (along-line) and transverse (perpendicular) offset distances. The linear array runs approximately S-N from the bottom to the top of the active lobe, so positive longitudinal offsets are to the north (up the slope) and positive transverse offsets are to the east (towards a gully between adjacent landslide lobes). To quantify the effects of these offsets we examine the ratio  $r_a$  of the measured apparent resistivity to its baseline value. This is calculated using the same geometric factor for the baseline and subsequent measurements; therefore  $r_a$  is also given by the ratio of the measured transfer resistances. We also use a simplified analytical expression to model  $r_a$  for electrode movements on the surface of a homogeneous half-space which also has a time-dependent resistivity. We denote the baseline distances between the electrodes A, B, M, and N to be  $AM$ ,  $BM$ ,  $AN$ , and  $BN$ , and the

distances at the later time to be  $AM'$ ,  $BM'$ ,  $AN'$ , and  $BN'$ . We also denote the ratio of the homogeneous half-space resistivities to be  $r = \rho'/\rho$ . The apparent resistivity ratio for the homogeneous half-space is then given by

$$r_a = r \left( \frac{\frac{1}{AM'} - \frac{1}{BM'} - \frac{1}{AN'} + \frac{1}{BN'}}{\frac{1}{AM} - \frac{1}{BM} - \frac{1}{AN} + \frac{1}{BN}} \right). \quad (1)$$

The effects of electrode movement and changing resistivity ratio are shown in Figure 6. The along-line electrode spacing is taken to be 4.75 m, and a particular electrode (in this case electrode 9 at 38 m) is offset from its assumed position. Figure 6a shows the effect of a longitudinal movement of 1 m on the apparent resistivities of the dipole-dipole configurations with  $a = 4.75$  m and  $n = 1 - 4$ . Similarly the effects of a 1 m transverse movement on the same configurations are shown in Figure 6b. It is clear that the linear dipole-dipole configuration is much more sensitive to longitudinal electrode movements than transverse. It can be seen by comparing Figure 6a with Figure 6c, which shows the effects of simultaneous 1 m longitudinal and transverse movements, that the effect of the transverse movements is typically negligible (with the exception of  $n = 1$  where the largest change is  $r_a \approx 1.6$  in Figure 6a, and  $r_a \approx 1.5$  in Figure 6c). In Figure 6d, the effects of changes in subsurface resistivity as well as electrode movements are shown. For each  $n$ -level we have used a different resistivity ratio  $r$  to approximate the effects of resistivity changes that vary with the depth-of-investigation (Barker 1989).

The sensitivity of a given configuration to longitudinal and transverse electrode movements can be calculated, in the case of a homogeneous half-space, from the expressions for the geometric factor

$$K = \frac{2\pi}{\frac{1}{AM} - \frac{1}{BM} - \frac{1}{AN} + \frac{1}{BN}} \quad (2)$$

and its total differential

$$dK = \frac{K^2}{2\pi} \left( \frac{dAM}{AM^2} - \frac{dBM}{BM^2} - \frac{dAN}{AN^2} + \frac{dBN}{BN^2} \right). \quad (3)$$

We consider the fractional changes in apparent resistivity  $|d\rho_a/\rho_a| = |dK/K|$  caused by small longitudinal ( $dl$ ) and transverse displacements ( $dt$ ) on the slope. In each case the displacements are expressed as fractions of the unit electrode spacing,  $a$ . The results show that  $|d\rho_a/\rho_a| \propto |dl/a|$ , but that  $|d\rho_a/\rho_a| \propto |dt/a|^2$ . Therefore for small displacements  $dl < a$  and  $dt < a$  it is clear that longitudinal offsets will cause greater changes than transverse offsets. We define displacement sensitivities in the longitudinal and transverse directions as  $S_l = |d\rho_a/\rho_a| / |dl/a|$  and  $S_t = |d\rho_a/\rho_a| / |dt/a|^2$  respectively. These are listed with their functional forms and numerical values for dipole-dipole and Wenner-Schlumberger configurations in Table 2 and Table 3 respectively.

It is interesting to note from Figure 6 that the magnitudes of the changes in  $r_a$  caused by longitudinal electrode movement do not vary rapidly with  $n$ . This can be understood by examining the longitudinal sensitivities in Table 2. For dipole-dipole configurations  $d\rho_a/\rho_a$  is only weakly dependent on  $n$  (in fact for large  $n$  it tends to a constant). Interestingly, for the Wenner-Schlumberger array  $d\rho_a/\rho_a$  varies approximately as  $1/n$  for displacements of the outer electrodes, although for the inner electrodes it again depends only weakly on  $n$  and tends to a constant. The results in Table 2 show that dipole-dipole measurements are somewhat more sensitive to longitudinal electrode displacements than Wenner-Schlumberger configurations, and hence are better suited to tracking movements of the electrodes using resistivity data.

**Table 2.** Sensitivity  $S_l = |d\rho_a/\rho_a| / |dl/a|$  of dipole-dipole and Wenner-Schlumberger configurations to longitudinal electrode movements

$n$	Dipole-Dipole		Wenner-Schlumberger	
	Outer electrodes $S_l = \frac{n(2n+3)}{2(n+1)(n+2)}$	Inner electrodes $S_l = \frac{(2n+1)(n+2)}{2n(n+1)}$	Outer electrodes $S_l = \frac{2n+1}{2n(n+1)}$	Inner electrodes $S_l = \frac{2(n^2+n)+1}{2n(n+1)}$
1	0.417	2.250	0.750	1.250
2	0.583	1.667	0.417	1.083
3	0.675	1.458	0.292	1.042
4	0.733	1.350	0.225	1.025
5	0.774	1.283	0.183	1.017
6	0.804	1.238	0.155	1.012
7	0.826	1.205	0.134	1.009
8	0.844	1.181	0.118	1.007

**Table 3.** Sensitivity  $S_t = |d\rho_a/\rho_a| / |dt/a|^2$  of dipole-dipole and Wenner-Schlumberger configurations to transverse electrode movements

$n$	Dipole-Dipole		Wenner-Schlumberger	
	Outer electrodes $S_t = \frac{n(3n^2+9n+7)}{4(n+1)^2(n+2)^2}$	Inner electrodes $S_t = \frac{(n+2)(3n^2+3n+1)}{4n^2(n+1)^2}$	Outer electrodes $S_t = \frac{3n^2+3n+1}{4n^2(n+1)^2}$	Inner electrodes $S_t = \frac{3n^2+3n+1}{4n^2(n+1)^2}$
1	0.132	1.313	0.438	0.438
2	0.128	0.528	0.132	0.132
3	0.114	0.321	0.064	0.064
4	0.101	0.229	0.038	0.038
5	0.090	0.177	0.025	0.025
6	0.081	0.144	0.018	0.018
7	0.073	0.121	0.013	0.013
8	0.067	0.105	0.010	0.010

**Table 4.** Sensitivity  $S_h = |d\rho_a/\rho_a| / |dh/a|$  of dipole-dipole and Wenner-Schlumberger configurations to perpendicular deformations of the surface

$n$	Dipole-Dipole		Wenner-Schlumberger	
	Outer electrodes $S_h$	Inner electrodes $S_h$	Outer electrodes $S_h$	Inner electrodes $S_h$
1	0.070	0.062	0.033	0.092
2	0.180	0.086	0.009	0.142
3	0.192	0.101	0.010	0.152
4	0.192	0.111	0.009	0.156
5	0.191	0.118	0.008	0.158
6	0.190	0.124	0.006	0.160
7	0.188	0.128	0.005	0.161
8	0.186	0.132	0.005	0.162

Another possible source of electrode displacements on a landslide is perpendicular movement of the surface caused by e.g. rotational slips or the development of scarps. We have calculated the sensitivity of dipole-dipole and Wenner-Schlumberger configurations to small deformations ( $dh$ ) of the surface in the direction perpendicular to the slope using the R2 finite-element forward modelling code (Binley & Kemna 2005). The results were calculated for  $|dh/a| = 0.005, 0.01, 0.02$  &  $0.05$  and indicate that the sensitivity can be expressed as  $S_h = |d\rho_a/\rho_a| / |dh/a|$ . Table 4 gives  $S_h$  as a function of  $n$ , and comparison with Table 2 shows that the sensitivity to perpendicular deformation is approximately an order-of-magnitude less than the sensitivity to longitudinal displacement.

Having calculated the effects of electrode movements in a simplified analytical example, we used the same approach to examine the apparent resistivity ratios from the field measurements using the March 2009 and the baseline data sets. Figure 7a shows, in red, the measured apparent resistivity ratios and, in blue, the ratios calculated from the measured longitudinal movements (assuming no changes in the resistivity of the homogeneous half-space). Although the real resistivity distribution is clearly strongly heterogeneous, by using the ratio of the data the effects of the static heterogeneity are suppressed. This is similar to dividing by reference data to suppress 3D effects in 2D imaging (Ramirez & Daily 2001) and artefacts due to errors in electrode positions and boundary conditions (Gasulla *et al.* 2005). It also agrees with the findings of Zhou & Dahlin (2003) that electrode position errors cause similar effects in homogeneous and inhomogeneous models. The fit between the measured and calculated ratios is already good, with an RMS misfit error of 3.77 %. By including the measured transverse movements (Figure 7b) the fit is improved slightly to 3.69 %, with an obvious improvement only visible for the largest calculated

$r_a$  on the  $n = 1$  curve. Although static heterogeneity (i.e. spatial variation in subsurface resistivity) is suppressed by using ratio data, temporal variations in resistivity will affect the apparent resistivity ratio. To help account for these changes, as in Figure 6d, we include a bulk resistivity ratio  $r$  that varies as a function of the depth-of-investigation (i.e. effectively with the  $n$ -level for a fixed dipole length  $a$ ). This assumes that the time-lapse changes in resistivity are caused primarily by changes in temperature and saturation, and that these changes depend predominantly on depth. Note that changes in the resistivity distribution caused by mass movement may lead to spatially localised apparent resistivity changes that will not be well described by this term. But this is not expected to have a large effect in this case since the rate of lobe movement is quite slow (typically several decimetres per year). The use of a ratio term is appropriate here since resistivity is approximately proportional to saturation (Archie 1942) and inversely proportional to temperature (Hayley *et al.* 2007). The ratios were estimated simply by inspection of the measured and predicted data, and were found to be 1.00, 1.02, 1.03 and 1.03 for  $n = 1, 2, 3$  and 4 respectively. They are close to unity since the saturation and temperature conditions would have been similar in March 2009 to the baseline conditions in March 2008. In Figure 7c these resistivity ratios have been applied in addition to the measured movements. This has improved the RMS misfit to 2.62 %. It is clear from Figure 7a - c that the greatest effect on the apparent resistivity ratios is caused by the longitudinal electrode movements, followed by the depth-dependent changes in the subsurface resistivity. The effect of transverse movements is, apart for a small number of  $n = 1$  data, effectively negligible. By using the measured longitudinal electrode positions in the resistivity inversion, the subsurface image is significantly improved (as shown in Figure 7d and normalised to the baseline in Figure 7e). Comparison with Figure 4a and Figure 4b shows that the

anomalous resistivity structures have been removed, and the RMS misfit of the resistivity inversion has improved to 1.02 %, the same as for the baseline model. Note that the depth-dependent resistivity ratios are not used in the resistivity inversion; their purpose is only to improve the fit between the modelled and observed resistivity ratios by accounting, albeit in an approximate fashion, for changes caused by subsurface resistivity variations rather than by electrode movements.

The analysis of Figure 7 suggests that it should be possible to recover the longitudinal electrode offsets from time-lapse resistivity data by fitting the observed apparent resistivity ratios to those calculated for a homogeneous half-space. But the data were obtained under similar conditions to the baseline and so represent a nearly ideal case. It is important to examine how well or otherwise the calculated  $r_a$  fit the data when saturation and temperature conditions differ from the baseline. Figure 8 presents an analysis of the August 2009 data using the same approach. The calculated  $r_a$  (blue lines) are identical to those for March 2009 since it is assumed that no movement occurred between these times (as noted earlier, movement of the lobe typically occurs in January and February). The observed  $r_a$  (red lines) are considerably “noisier” than those in Figure 7, although this is likely to be due to changes in the resistivity distribution of the landslide as well as the observed increase in random noise (see Table 1). Despite less ideal conditions, the August  $r_a$  data show similar behaviour to the March data; the RMS misfit values are higher but the measured longitudinal movements seem to account for the gross features in the observed  $r_a$  values (Figure 8a). As in Figure 7, the fit improves slightly with the correction of the transverse offsets (Figure 8b), but is better still with the inclusion of estimated depth-dependent resistivity ratios ( $r = 0.89, 0.93, 0.96, 0.98$  for  $n = 1, 2, 3$  and 4 respectively, see Figure 8c). Again, correcting the longitudinal electrode

positions removed the anomalies in the resistivity image, and reduced the RMS misfit of the resistivity inversion to, in this case, 1.07 % (see Figure 8d and Figure 8e). The normalised resistivity image (Figure 8e) reveals a distinct layering. We speculate that the resistivity reduction in the top ~3 m of the image is due to the increased subsurface temperature compared to the baseline. Only 5.5 mm rain fell at the site in the week preceding the collection of the August 2009 data; therefore it seems unlikely that increased saturation would account for these resistivity decreases relative to the baseline conditions. It seems more probable that the saturation has decreased throughout the top ~10 m of the subsurface, leading to the observed increase in resistivity in the lower layer, and that this has been masked by the greater effect of increased temperature in the top ~3 m. Some supporting evidence for this interpretation is provided by ongoing temperature monitoring at the site, which indicates an average thermal diffusivity in the range 0.03 - 0.06 m<sup>2</sup>/day, giving an average characteristic depth of penetration of 1.9 - 2.7 m for surface temperature fluctuations.

## **Electrode position inversion**

The preceding analysis shows that uncorrected movements in the longitudinal positions of electrodes on a linear ERT array cause significant artefacts in apparent resistivity data and the resulting inverted images. If these position offsets are measured and corrected, then the artefacts are removed and images of similar quality to those of the baseline can be recovered. Even in the presence of noise, the results suggest that a model based on longitudinal electrode movements on a homogeneous half-space combined with depth-dependent time-lapse resistivity changes can be used to predict the observed artefacts. By using the ratios of the observed data to the baseline, the effects of subsurface heterogeneity seem to be sufficiently suppressed to

make inverting for the longitudinal electrode offsets a possibility using this simplified analytical model.

To test this hypothesis we attempt to find the vectors of longitudinal electrode movements  $\mathbf{m}$  and depth-dependent resistivity ratios  $\mathbf{r}$  that minimise the merit function

$$f = \sqrt{\sum_i |e_i|^2} + \alpha \sum_j |m_j| + \beta \sum_j \theta(m_j) |m_j|, \quad (4)$$

where  $\mathbf{e} = \mathbf{r}_{a,pre} - \mathbf{r}_{a,obs}$  is the data discrepancy vector between the predicted apparent resistivity ratios calculated from eq. 1 and the observed ratios,  $\alpha$  and  $\beta$  are the weights of the model constraints, and  $\theta$  is the Heaviside step function. The first term of the merit function imposes an  $L_2$ -norm constraint on the data discrepancy, the second term is an  $L_1$ -norm damping constraint on the length of the movement vector, and the third term applies a negativity constraint to the elements of the movement vector (the electrodes should move towards the origin, i.e. downhill). Note that the elements of  $\mathbf{r}$  are allowed to vary freely without constraint. We minimise  $f$  using the FindMinimum[] function in the Mathematica computational algebra software. This is a Quasi-Newton method which uses the BFGS algorithm to update the approximated Hessian matrix (Press *et al.* 1992). Convergence was judged to have occurred when the relative change in  $f$  between subsequent iterations was  $<1\%$ .

The results of this approach for the March 2009 data are shown in Figure 9a. The red line shows the measured longitudinal electrode movements, the blue line shows the movements predicted by minimising  $f$ . To obtain these results we used weights of  $\alpha = 0.06 \text{ m}^{-1}$  and  $\beta = 0.32 \text{ m}^{-1}$  in eq. 4. The fit to the data is shown in Figure 9b for  $a = 4.75 \text{ m}$  and  $n = 2 - 4$ . The  $n = 1$  data is shown for completeness, but they were not used in the prediction of the longitudinal movements or the calculation of the RMS misfit since their sensitivity to transverse movements, although weak,

cannot be neglected. The fitted depth-dependent resistivity ratios are also shown and agree very closely with those estimated by inspection in Figure 7c (the ratio for  $n = 1$  is taken from the Figure 7 estimate). The fit between the observed and predicted data is very good, with an RMS misfit of 1.82 %. The predicted electrode positions are all within 0.2 m (or 4 % of the unit electrode spacing) of their measured positions. Using the predicted electrode positions in the resistivity inversion produces an RMS misfit of 1.06 %, very close to that achieved using the measured positions. The resulting resistivity image (Figure 9c and Figure 9d) is also extremely similar (cf. Figure 7d and Figure 7e) and does not exhibit the anomalies that were present before the electrode positions were corrected (Figure 4a and Figure 4c).

For the August 2009 data, levels of random noise and heterogeneous resistivity changes were greater, therefore the model constraint weighting factors were increased to  $\alpha = 0.08 \text{ m}^{-1}$  and  $\beta = 0.40 \text{ m}^{-1}$ . Despite this, the electrode positions could still be predicted to approximately the same level of accuracy. The predicted movements are shown in Figure 10a, and again are all within 0.2 m of the measured positions, although the number of larger discrepancies (in the range 0.1 - 0.2 m) has increased from 3 for the March data to 6. The fit to the data (as shown in Figure 10b) is reasonable, with an RMS misfit of 6.54 %. Once again, the fitted depth-dependent resistivity ratios agree very closely with those in Figure 8c, and the inverted resistivity image (Figure 10c and Figure 10d) is very similar to that for the measured electrode positions (Figure 8d and Figure 8e). While the RMS misfit of the resistivity inversion is slightly higher (1.15 % cf. 1.07 %), it is better than that of the uncorrected inversion (at 1.46 %).

## Discussion

The above example has demonstrated that electrode movements on an active landslide can be recovered by inverting time-lapse geoelectrical data using a simplified analytical forward model. Whilst the primary intention of this study is as a proof-of-concept, we also aim to discuss some aspects of the general applicability of the method, namely the sensitivity of the inversion to the regularisation constraints; the applicability of the method in regions of stronger heterogeneity; and its applicability in regions of more rugged topography.

The model damping ( $\alpha$ ) and negativity ( $\beta$ ) constraints were chosen to minimise the misfit between the inverted and the measured longitudinal movements. Generally, however, the measured positions would not be available when predicting electrode movements using this technique. Therefore it is desirable to assess the sensitivity of the results to the regularisation parameters. Figure 11 shows the mean misfit between the inverted and measured electrode movements as functions of  $\alpha$  and  $\beta$  for the March 2009 data. The values highlighted by the vertical arrows ( $\alpha = 0.06 \text{ m}^{-1}$ ,  $\beta = 0.32 \text{ m}^{-1}$ ) were used to generate Figure 9, but similar results would have been obtained for  $0.01 \text{ m}^{-1} < \alpha < 0.10 \text{ m}^{-1}$  and for  $\beta > 0.30 \text{ m}^{-1}$ . The insets in Figure 11a show that if the inversion is underdamped (e.g.  $\alpha = 0 \text{ m}^{-1}$ ) then large movements are accurately recovered, but nearly all electrodes with small or no movement are assigned spurious displacements of between 0.1 and 0.6 m. Conversely if the inversion is overdamped (e.g.  $\alpha = 0.25 \text{ m}^{-1}$ ) then the electrodes that do not move are correctly predicted, but the movements of the others are underestimated by up to 0.6 m. In Figure 11b, the insets show that if the negativity constraint is too small, then spurious upslope movements can be predicted. Larger values of  $\beta$  produce results very similar to those in Figure 9a, which is to be expected since none of the electrodes

actually moved upslope. However, it is possible in some cases that local upslope movement could actually occur (e.g. as a result of a rotational slip). It is likely that these displacements could be predicted by the inversion, since small upslope displacements can result even when  $\beta > 0$  (e.g. see electrode 8 in Figure 9a). But the range of  $\beta$  that produced good predictions would have an upper limit in such cases, and it might be worth experimenting with different regularisation schemes instead (e.g. smoothness constraints (Loke *et al.* 2003) on adjacent electrode displacements).

The position inversion method depends on approximating the movement-induced changes in apparent resistivity ratios using a model with a homogeneous subsurface. In the preceding case history, the moving electrodes are being carried by a lobe of mudstone slipping over underlying sandstone with a resistivity contrast of approximately an order-of-magnitude. The thickness of the lobe in the resistivity images is  $\sim 5$  m, which is similar to the maximum median depth-of-investigation of the data used to invert the electrode positions (for  $a = 4.75$  m and  $n = 4$ , the median depth-of-investigation  $z_{1,4} = 5.8$  m). To investigate the effects of stronger static heterogeneity on resistivity ratio data and on the resulting position inversion, we consider two simple models: a vertically faulted half-space (Figure 12a) and a vertically faulted half-space with a covering layer of thickness  $z_{1,4}$  (Figure 12b). The apparent resistivities were calculated using the method of images for the faulted half-space (Patella 1997) and using the Res2DMod forward modelling software for the covered faulted half-space. The electrode spacing  $a = 4.5$  m was chosen to simplify the model discretisation; this spacing giving a corresponding  $z_{1,4} = 5.5$  m. In each case, the electrode immediately to the right of the fault at  $x = 2.25$  m was moved in the  $-x$  direction i) closer to the fault (red arrows and ratio curves) and ii) across the fault (blue arrows and ratio curves). The ratio curves are shown in Figure 12 for  $a =$

4.5 m,  $n = 1$  only, but all the data for  $n = 1 - 4$  were used to invert for the electrode position. In each case the method was tested for resistivity contrasts of  $\rho_2/\rho_1 = 0.001, 0.01, 0.1, 1, 10, 100,$  and  $1000,$  although for clarity the data are only shown for contrasts of  $0.1, 1,$  and  $10.$  The results of the position inversion for the displaced electrode in the two models are shown in Table 5 and Table 6. The results suggest that the method can be applied with good success (i.e. recovering electrode positions to within 4 % of the unit electrode spacing) providing either i) that the movement does not cause the electrode to cross a resistivity boundary or ii) that the electrode is carried across a boundary by a moving layer of thickness comparable to the depth-of-investigation of the data used in the inversion. If either of these conditions is met, then these results suggest that the position inversion will work well even in the presence of resistivity contrasts of up to three orders-of-magnitude.

**Table 5.** Inverted electrode positions,  $x,$  from a vertically faulted half-space model with contrast  $\rho_2/\rho_1$

$\rho_2/\rho_1$	<b>Actual <math>x</math></b>	Inverted $x$	<b>Actual <math>x</math></b>	Inverted $x$
0.001	<b>0.75</b>	0.93	<b>-0.75</b>	-2.24
0.01	<b>0.75</b>	0.93	<b>-0.75</b>	-2.19
0.1	<b>0.75</b>	0.90	<b>-0.75</b>	-1.77
1	<b>0.75</b>	0.75	<b>-0.75</b>	-0.75
10	<b>0.75</b>	0.63	<b>-0.75</b>	-0.35
100	<b>0.75</b>	0.61	<b>-0.75</b>	-0.30
1000	<b>0.75</b>	0.61	<b>-0.75</b>	-0.30

**Table 6.** Inverted electrode positions,  $x,$  from a covered vertically faulted half-space model with contrast  $\rho_2/\rho_1$

$\rho_2/\rho_1$	<b>Actual <math>x</math></b>	Inverted $x$	<b>Actual <math>x</math></b>	Inverted $x$
0.001	<b>0.75</b>	0.61	<b>-0.75</b>	-0.85
0.01	<b>0.75</b>	0.62	<b>-0.75</b>	-0.84
0.1	<b>0.75</b>	0.67	<b>-0.75</b>	-0.81
1	<b>0.75</b>	0.75	<b>-0.75</b>	-0.75
10	<b>0.75</b>	0.75	<b>-0.75</b>	-0.75
100	<b>0.75</b>	0.75	<b>-0.75</b>	-0.77
1000	<b>0.75</b>	0.74	<b>-0.75</b>	-0.77

A further approximation used in the position inversion is that the apparent resistivity ratios are modelled assuming a flat surface. This should be valid providing that the topography is locally close to flat, i.e. undulating by  $<10^\circ$  (Tsourlos *et al.* 1999) on the length scale of the electrode configurations being used. However landslides often exhibit more rugged topography than this. In these cases it is likely that significant errors in the inverted positions would be caused by using the flat half-space model. It might be possible to use a finite element modelling code to include the effects of topography, e.g. R2 (Binley & Kemna 2005). However, if the topography changes significantly during the movement period, it is unlikely that this could be recovered as well as the longitudinal displacements. This is because, as already shown in Table 4, the data are approximately an order-of-magnitude less sensitive to deformations of the surface than to longitudinal displacements.

## **Conclusion**

If permanently deployed electrodes move from their assumed positions while they are being used for time-lapse resistivity monitoring, then artefacts will be introduced in the resulting images, degrading the quality of the fit to the data and obscuring the structure of the subsurface resistivity images. Therefore it is important to update the positions before the data is inverted to produce the image. Manual or automated resurveying of the electrodes locations for every time-lapse dataset would be costly and/or technically challenging.

However, we have shown that it is possible to extract the electrode movements from the geoelectrical data and then use these to correct their positions in the resistivity inversion. Under certain circumstances (e.g. if the electrodes are being carried progressively downslope by a body of displaced material such as in a slide, spread or flow) using the ratios of the apparent resistivities to those of the baseline

data can suppress the effects of static heterogeneities in the resistivity distribution. This allows the effects of electrode movement to be calculated from an analytical homogeneous half-space model. In these situations, the apparent resistivity ratios do not depend strongly on the resistivity distribution (only on the time-lapse changes between distributions), and the analytical model can be used to invert for the electrode position offsets by making simplifying assumptions about the nature of the time-lapse changes in the resistivity distribution (in this case that they are a function of depth only).

We demonstrated this technique using data from a permanently installed linear electrode array running up an active lobe of a landslide. Two different time-lapse datasets were used that had a common baseline. The first set was acquired a year after the baseline under similar temperature and saturation conditions and represented a close-to-ideal case. The second set was taken 5 months later, and showed greater and more heterogeneous time-lapse variations in the recorded apparent resistivity data. However, in both cases the simple position inversion routine was able to predict the electrode displacements to within 0.2 m, or 4 % of the electrode spacing. Using the predicted positions in the subsequent resistivity inversion improved the fit to the data and removed the image artefacts that had been caused by assuming that the electrodes had not moved.

We aim to use this technique to track the electrode movements during the next period of landslide movement. Our research is ongoing into using series of time-lapse datasets to constrain the evolution of the position offsets to be a smooth function of time. While the research presented here addresses movements parallel to the linear array, we will also investigate using measurements in the perpendicular direction to determine transverse offsets as well. This would enable us to use similar techniques to

track the electrode movements in 2D, allowing for position-corrected 4D (i.e. 3D + time-lapse) inversion. The ultimate goal of this research is to combine the resistivity and position inversions into one algorithm, similar to those under development for use in medical electrical impedance tomography. This would enable the simultaneous reconstruction of the resistivity image and electrode positions in more complex situations with stronger transient heterogeneity and more rugged topography.

## Acknowledgements

We would like extend our sincerest gratitude to Mr. and Mrs. Gibson (the landowners) for their involvement and cooperation in this research. We also thank the editor (Dr Mark Everett) and two anonymous reviewers for their helpful comments on our original manuscript. This paper is published with permission of the Executive Director of the British Geological Survey (NERC).

## References

Archie, G.E., 1942. The electrical resistivity log as an aid in determining some reservoir characteristics, *Petroleum Trans. AIME.*, **146**, 54–62.

Barker, R.D., 1989. Depth of investigation of collinear symmetrical four-electrode arrays, *Geophysics*, **54**, 1031–1037.

Binley, A. & Kemna A., 2005. *Electrical Methods*, In: Hydrogeophysics by Rubin & Hubbard (Eds.), 129-156, Springer.

Blott, B.H., Daniell, G.J. & Meeson, S., 1998. Electrical impedance tomography with compensation for electrode positioning variations, *Phys. Med. Biol.*, **43**, 1731–1739.

British Geological Survey, 1983. York solid and drift (Sheet 63). 1:50 000. Keyworth, Nottingham: *British Geological Survey*.

Chambers, J.E., Meldrum, P.I., Gunn, D.A., Wilkinson, P.B., Kuras, O., Weller, A.L., & Ogilvy, R.D., 2009. Hydrogeophysical monitoring of landslide processes using automated time-lapse electrical resistivity tomography (ALERT), *Proc. 15<sup>th</sup> EAGE Near Surf. Geophys. Meeting, Dublin, Ireland*.

Cruden, D.M. & Varnes, D.J., 1996. Landslide types and processes. In: A.K. Turner and R.L. Schuster (Editors), Special Report 247: Landslides, Investigation and Mitigation. National Academy Press, Washington DC, pp. 36-71.

Dai, T., Gómez-Laberge, C. & Adler, A., 2008. Reconstruction of conductivity changes and electrode movements based on EIT temporal sequences, *Physiol. Measur.*, **29**, S77–S88.

Friedel, S., Thielen, A. & Springman, S.M., 2006. Investigation of a slope endangered by rainfall-induced landslides using 3D resistivity tomography and geotechnical testing, *J. Appl. Geophys.*, **60**, 100-114.

Gasulla, M. & Pallàs-Areny, 2005. R. Noniterative algorithms for electrical resistivity imaging applied to subsurface local anomalies, *IEEE Sensors J.*, **5**, 1421–1432.

Gómez-Laberge, C. & Adler, A., 2008. Direct EIT Jacobian calculations for conductivity change and electrode movement, *Physiol. Measur.*, **29**, S89–S99.

Hayley, K., Bentley, L.R., Gharibi, M. & Nightingale, M., 2007. Low temperature dependence of electrical resistivity: Implications for near surface geophysical monitoring, *Geophys. Res. Lett.*, **34**, L18402.

Jomard, H., Lebourg, T., Binet, S., Tric, E., & Hernandez, M., 2007. Characterization of an internal slope movement structure by hydrogeophysical surveying, *Terra Nova*, **19**, 48-57.

Jongmans, D. & Garambois, S., 2007. Geophysical investigation of landslides : a review, *Bull. Soc. Géol. Fr.*, **178**, 101-112.

Kuras, O., Pritchard, J.D., Meldrum, P.I., Chambers, J.E., Wilkinson, P.B., Ogilvy, R.D. & Wealthall, G.P., 2009. Monitoring hydraulic processes with automated time-lapse electrical resistivity tomography (ALERT), *C. R. Geoscience*, **341**, 868-885.

Lapenna, V., Lorenzo, P., Perrone, A., Piscitelli, S., Rizzo, E. & Sdao, F., 2005. 2D electrical resistivity imaging of some complex landslides in the Lucanian Apennine chain, southern Italy, *Geophysics*, **70**, B11-B18.

Lebourg, T., Binet, S., Tric, E., Jomard, H. & El Bedoui, S., 2005. Geophysical survey to estimate the 3D sliding surface and the 4D evolution of the water pressure on part of a deep seated landslide, *Terra Nova*, **17**, 399-406.

Lebourg, T., Hernandez, M.H., El Bedoui, S.E.L. & Jomard, H.L., 2009. Statistical analysis of the Time Lapse Electrical Resistivity Tomography of the “Vence landslide” as a tool for prediction of landslide triggering, *Proc. EGU Gen. Assem., Vienna, Austria*

Li, X.F., Luo, C.Y., Wang, P., Chen, M.Y. & He, W., 2008. Using genetic algorithm for electrode movement problem in electrical impedance tomography. *Proc. World Automation Congr.*, 1804-1807.

Loke, M.H., Acworth, I. & Dahlin, T., 2003. A comparison of smooth and blocky inversion methods in 2-D electrical imaging surveys, *Explor. Geophys.*, **34**, 182–187.

Meric, O., Garambois, S., Jongmans, D., Wathelet, M., Chatelain, J.L., Vengeon, J.M., 2005. Application of geophysical methods for the investigation of the large gravitational mass movement of Sechilienne, France, *Can. Geotech. J.*, **42**, 1105-1115.

Naudet, V., Lazzari, M., Perrone, A., Loperte, A., Piscitelli, S. & Lapenna, V., 2008. Integrated geophysical and geomorphological approach to investigate the snowmelt-triggered landslide of Bosco Piccolo village (Basilicata, southern Italy), *Eng. Geol.*, **98**, 156-167.

Ogilvy, R.D., Meldrum, P.I., Kuras, O., Wilkinson, P.B., Chambers, J.E., Sen, M., Pulido-Bosch, A., Gisbert, J., Jorreto, S., Frances, I. & Tsourlos, P., 2009. Automated

monitoring of coastal aquifers with electrical resistivity tomography, *Near Surf. Geophys.*, **7**, 367-375.

Oldenborger, G.A., Routh, P.S. & Knoll, M.D., 2005. Sensitivity of electrical resistivity tomography data to electrode position errors, *Geophys. J. Int.*, **163**, 1–9.

Patella, D., 1997. Introduction to ground surface self-potential tomography, *Geophysical Prospecting*, **45**, 653-681.

Parasnis, D.S., 1988. Reciprocity theorems in geoelectric and geoelectromagnetic work, *Geoexploration*, **25**, 177–198.

Piegari, E., Cataudella, V., Di Maio, R., Milano, L., Nicodemi, M. & Soldovieri, M.G., 2009. Electrical resistivity tomography and statistical analysis in landslide modelling: A conceptual approach, *J. Appl. Geophys.*, **68**, 151-158.

Perrone, A., Iannuzzi, A., Lapenna, V., Lorenzo, P., Piscitelli, S., Rizzo, E. & Sdao, F., 2004. High-resolution electrical imaging of the Varco d'Izzo earthflow (southern Italy), *J. Appl. Geophys.*, **56**, 17-29.

Press, W.H., Teukolsky, S.A., Vetterling, W.T. & Flannery, B.P., 1992. *Numerical Recipes in C: The Art of Scientific Computing*, 2nd edn, Cambridge University Press, Cambridge.

Ramirez, A. & Daily, W., 2001. Electrical imaging at the large block test—Yucca Mountain, Nevada, *J. Appl. Geophys.*, **46**, 85-100.

Sass, O., Bell, R. & Glade, T., 2008. Comparison of GPR, 2D-resistivity and traditional techniques for the subsurface exploration of the Öschingen landslide, Swabian Alb (Germany), *Geomorphology*, **93**, 89-103.

Soleimani, M., Gómez-Laberge, C. & Adler, A., 2006. Imaging of conductivity changes and electrode movement in EIT, *Physiol. Measur.*, **27**, S103–S113.

Supper, R., Römer, A., Jochum, B., Bieber, G. & Jaritz, W., 2008. A complex geoscientific strategy for landslide hazard mitigation – from airborne mapping to ground monitoring, *Adv. Geosci*, **14**, 195-200.

Suzuki, K. & Higashi, S., 2001. Groundwater flow after heavy rain in landslide-slope area from 2-D inversion of resistivity monitoring data, *Geophysics*, **66**, 733-743.

Tsourlos, P.I., Syzmanski, J.E. & Tsokas, G.N., 1999. The effect of terrain topography on commonly used resistivity arrays, *Geophysics*, **64**, 1357-1363.

Wilkinson, P.B., Chambers, J.E., Lelliott, M., Wealthall, G.P. & Ogilvy, R.D., 2008. Extreme sensitivity of crosshole electrical resistivity tomography measurements to geometric errors, *Geophys. J. Int.*, **173**, 49–62.

Zhang, J. & Patterson, R.P., 2005. EIT images of ventilation: what contributes to the resistivity changes?, *Physiol. Measur.*, **26**, S81–S92.

Zhou, B. & Dahlin, T., 2003. Properties and effects of measurement errors on 2D resistivity imaging surveying, *Near Surf. Geophys.*, **1**, 105–117.

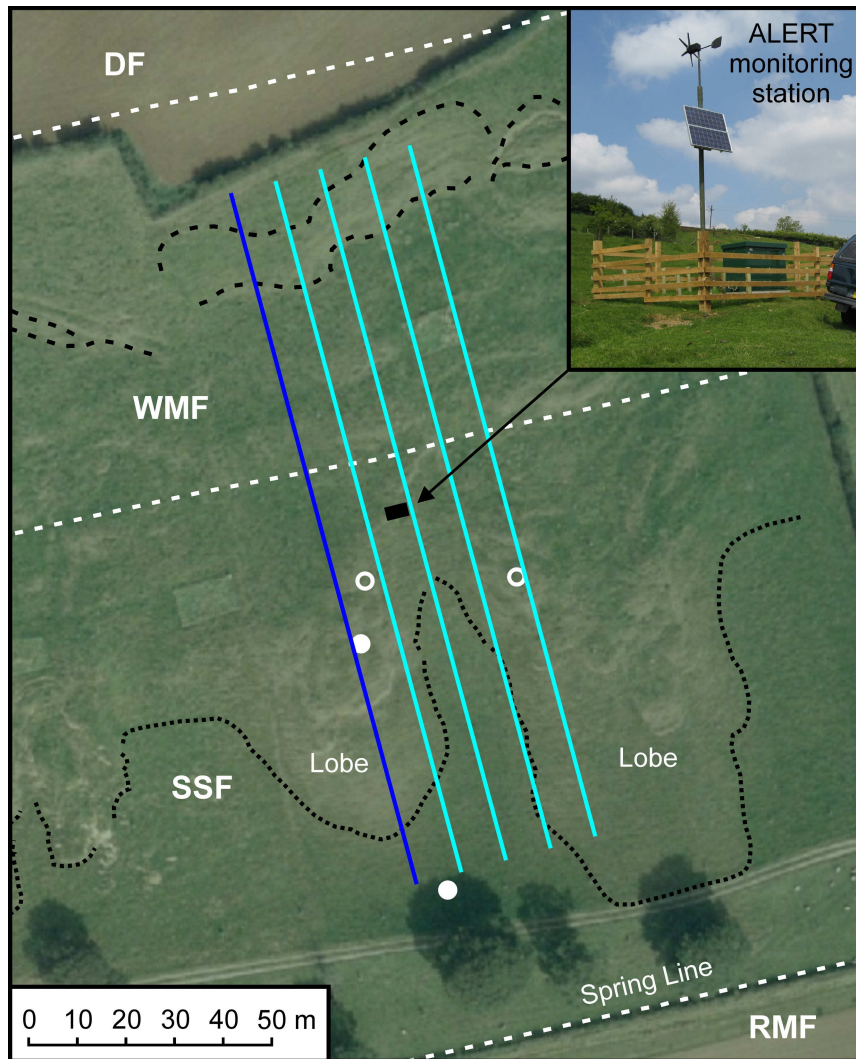


**Figure 1.** Site plan showing the location of the ALERT station, ERT monitoring arrays (dark and light blue lines), major geomorphologic features (top and base of the main scarp - black dashed lines; toe of the earth flows – dotted black lines) and bedrock geological boundaries (white dashed lines) between the Dogger Sandstone (DF), Whitby Mudstone (WMF), Staithes Sandstone (SSF) and Redcar Mudstone (RMF) formations. Borehole and piezometer locations are shown by filled and open circles respectively. (Aerial Photo © UKP/Getmapping Licence No. UKP2006/01)

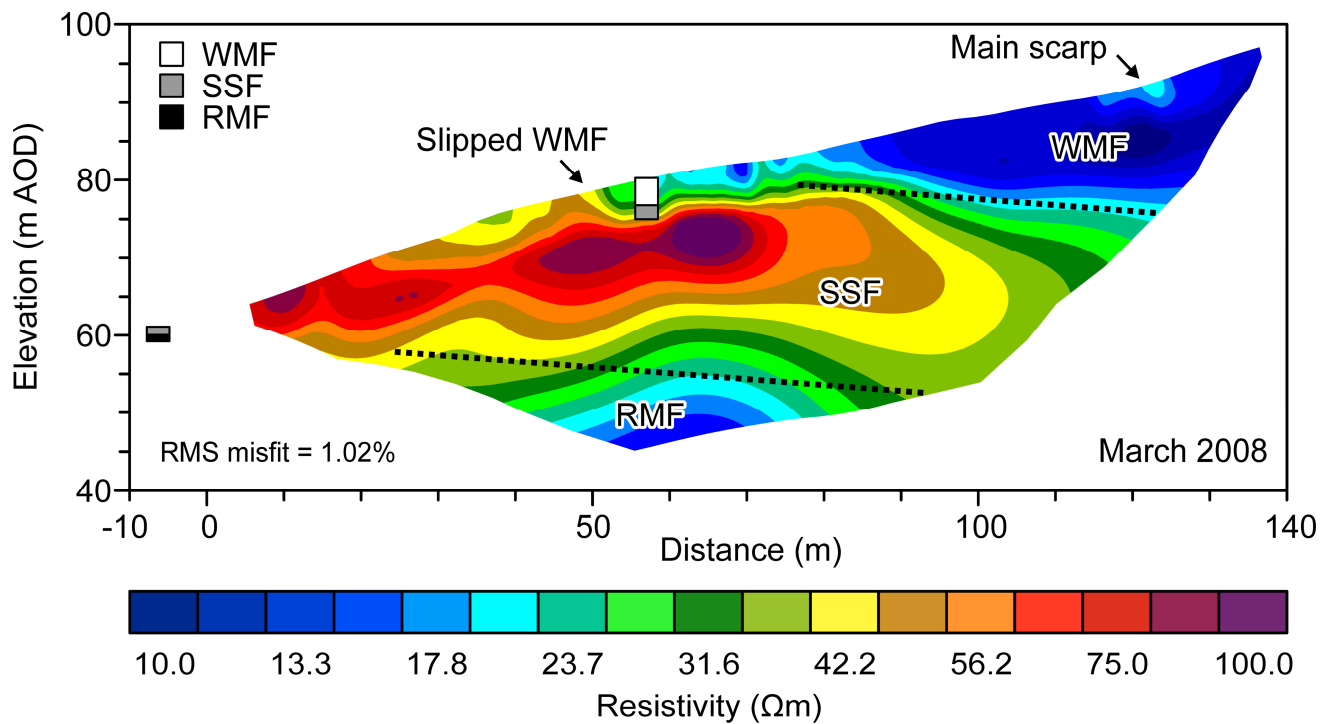


**Figure 2.** 2D resistivity image inverted from the baseline data set (March 2008). The inferred boundaries between the Whitby (WMF), Staithes (SSF) and Redcar (RMF) formations are shown by dotted black lines. Stratigraphic logs of boreholes are shown in greyscale. The main scarp and slipped WMF material are indicated by the black arrows.

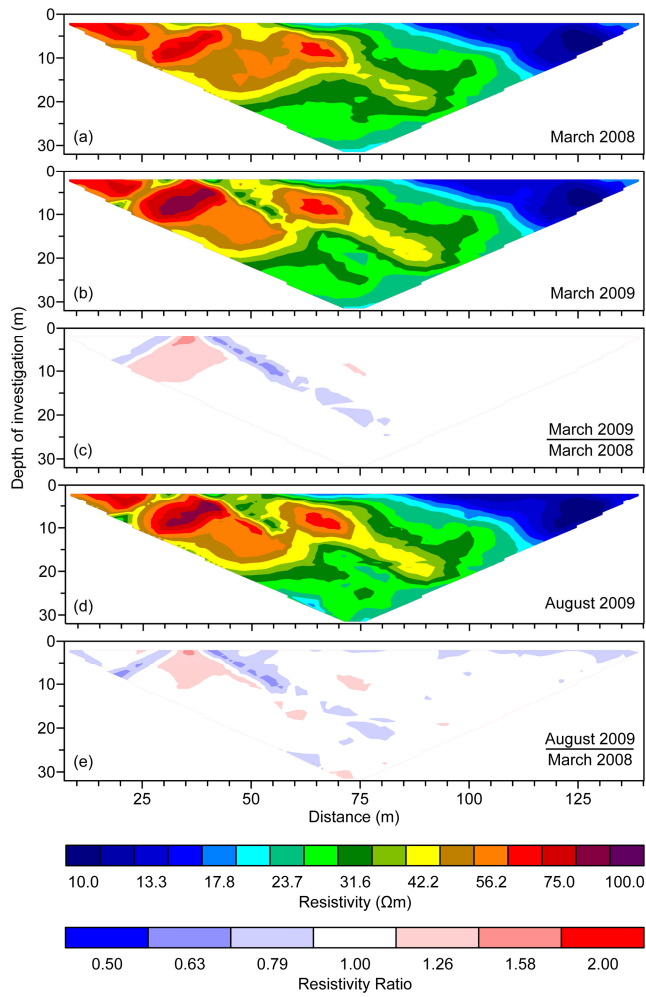


**Figure 3.** Raw data shown as resistivity and resistivity ratio pseudosections for (a) March 2008 (baseline), (b) & (c) March 2009, (d) & (e) August 2009.

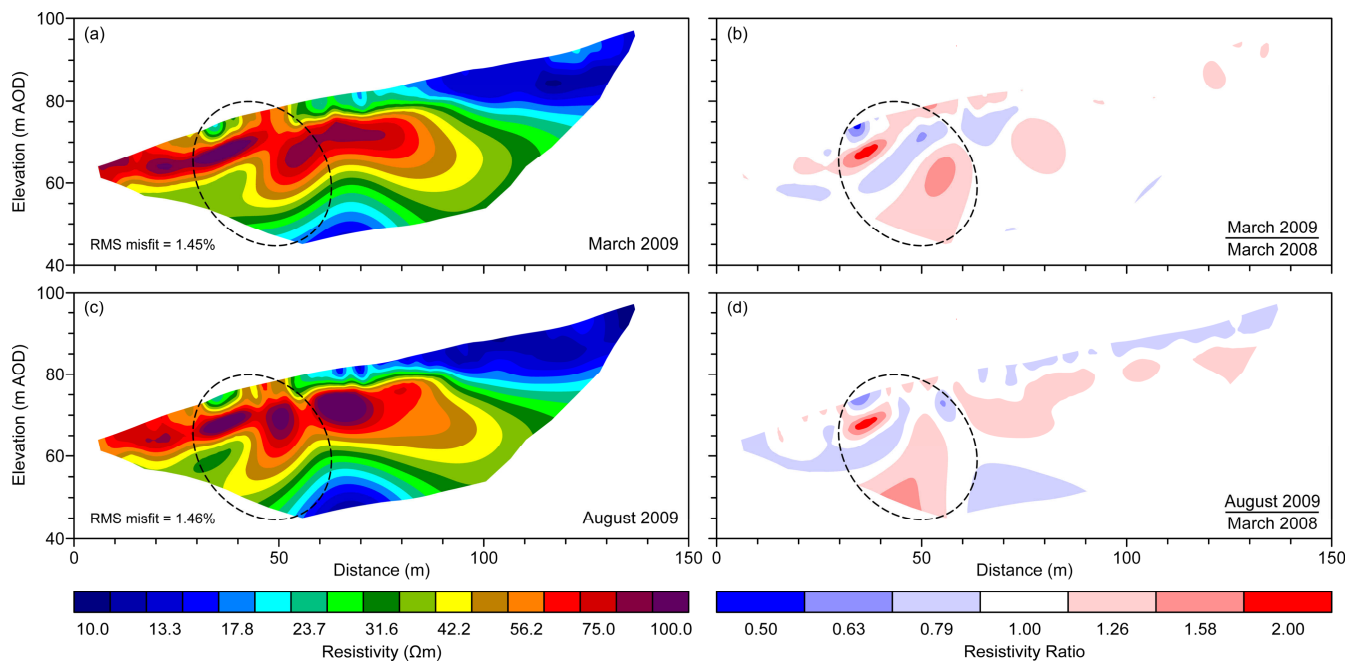


**Figure 4.** 2D resistivity image inverted from the uncorrected (a) March 2009 and (c) August 2009 data sets. The images are shown normalised to the baseline image in (b) and (d). Anomalous features are highlighted by dashed ellipses.

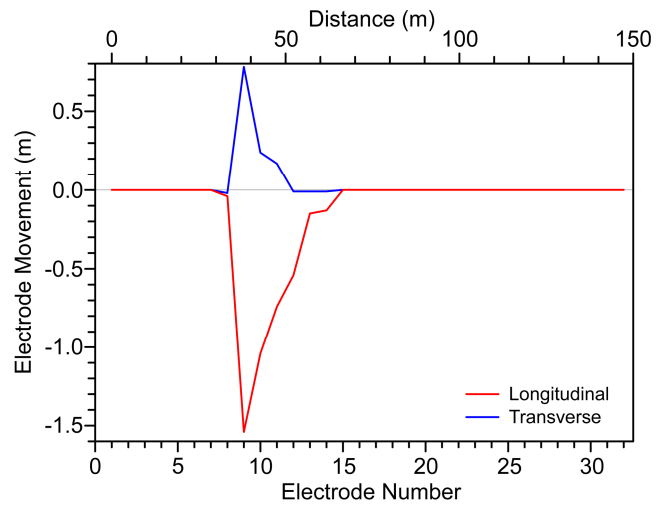


**Figure 5.** Changes in electrode positions between March 2008 and August 2009, shown as longitudinal (red) and transverse (blue) offset distances.

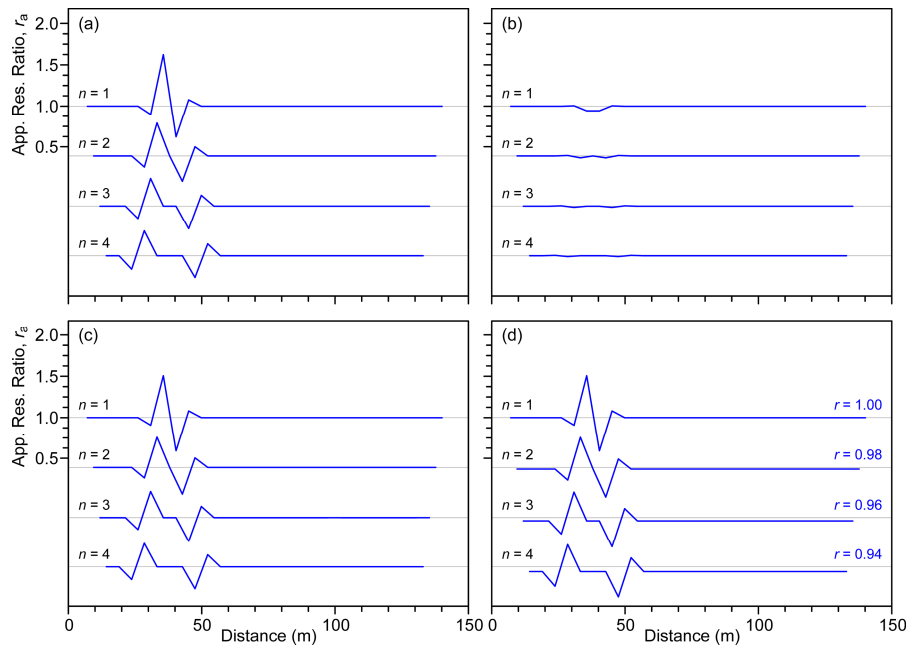


**Figure 6.** Effects on the apparent resistivity ratio of (a) longitudinal electrode movement, (b) transverse electrode movement, (c) longitudinal and transverse movement, (d) longitudinal and transverse movement and depth-of-investigation dependent resistivity ratio  $r$ . Data are plotted against configuration midpoint distance for  $a = 4.75$  m and  $n = 1 - 4$ .  $r_a$  curves for subsequent  $n$ -levels are shown offset for clarity; for each  $n$  the light grey horizontal axis indicates  $r_a = 1$ .

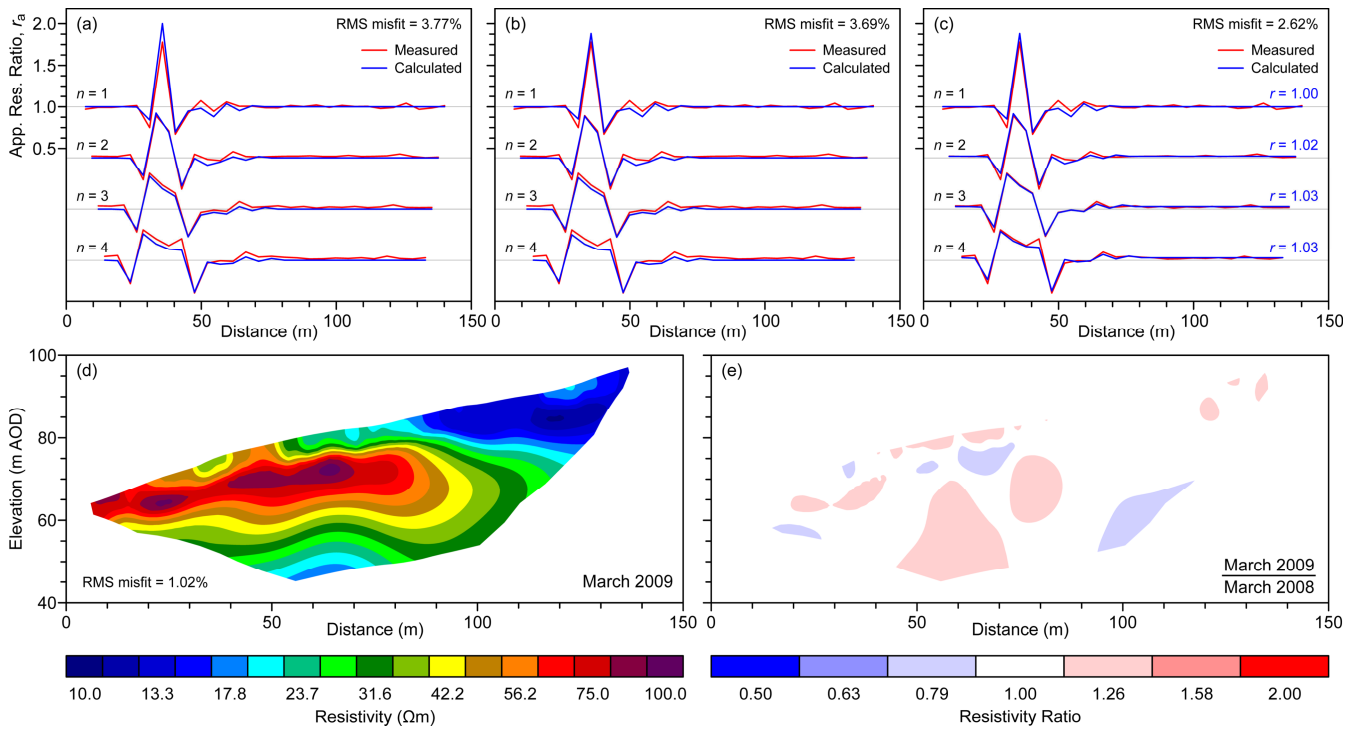


**Figure 7.** March 2009 apparent resistivity ratios and inverted images. Measured apparent resistivity ratios (red) and calculated ratios (blue) for (a) measured longitudinal movement only, (b) measured longitudinal and transverse movement, and (c) measured longitudinal and transverse movement and estimated depth-dependent resistivity ratio  $r$ . Data are shown for  $a = 4.75$  m and  $n = 1 - 4$ . For each  $n$ -level the light grey horizontal axis indicates  $r_a = 1$ . (d) and (e) Resistivity and normalised resistivity images obtained after measured longitudinal position corrections.

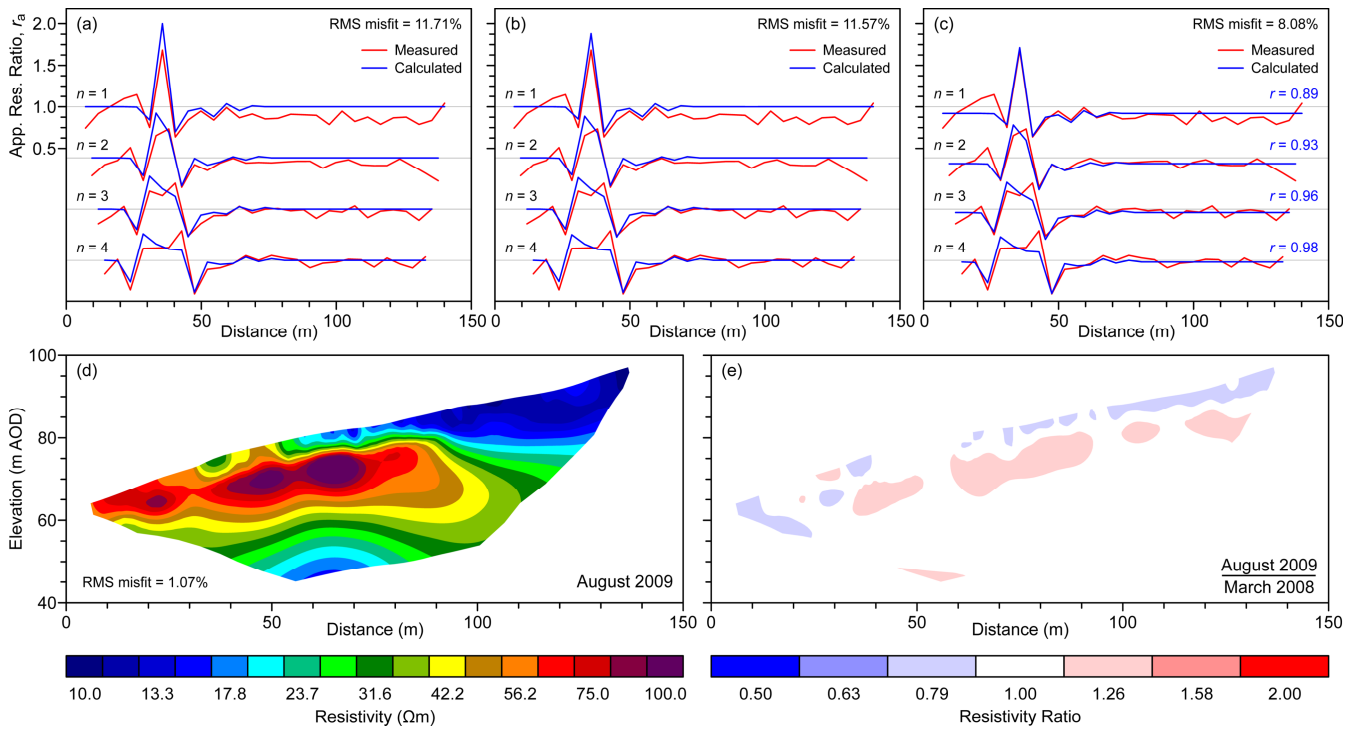


**Figure 8.** August 2009 apparent resistivity ratios and inverted images. Measured apparent resistivity ratios (red) and calculated ratios (blue) for (a) measured longitudinal movement only, (b) measured longitudinal and transverse movement, and (c) measured longitudinal and transverse movement and estimated depth-dependent resistivity ratio  $r$ . Data are shown for  $a = 4.75$  m and  $n = 1 - 4$ . For each  $n$ -level the light grey horizontal axis indicates  $r_a = 1$ . (d) and (e) Resistivity and normalised resistivity images obtained after measured longitudinal position corrections.

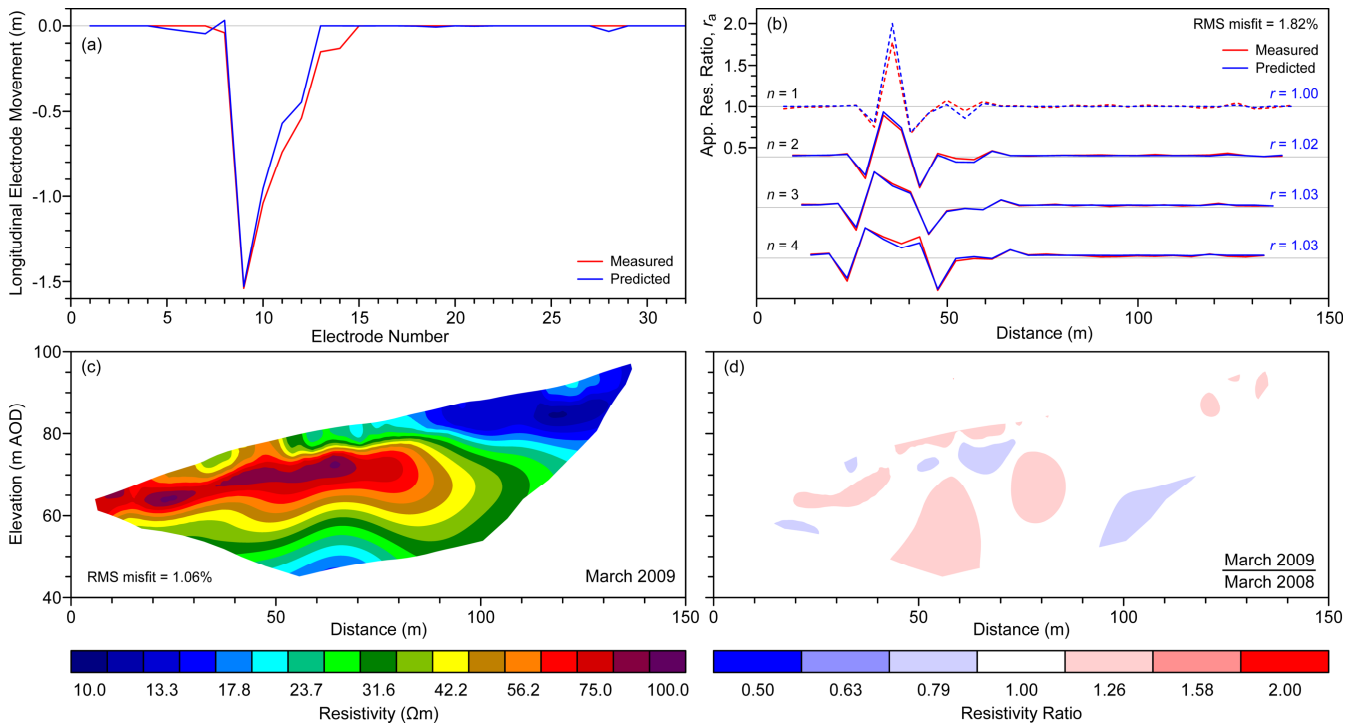


**Figure 9.** March 2009 (a) measured (red) and predicted (blue) longitudinal electrode movements. (b) measured (red) and predicted (blue) apparent resistivity ratios and depth-dependent resistivity ratios  $r$  (Data fitted to  $a = 4.75$  m and  $n = 2 - 4$ . Dashed lines show data not used in fit. For each  $n$ -level the light grey horizontal axis indicates  $r_a = 1$ ). (d) and (e) Resistivity and normalised resistivity images obtained after predicted longitudinal position corrections.

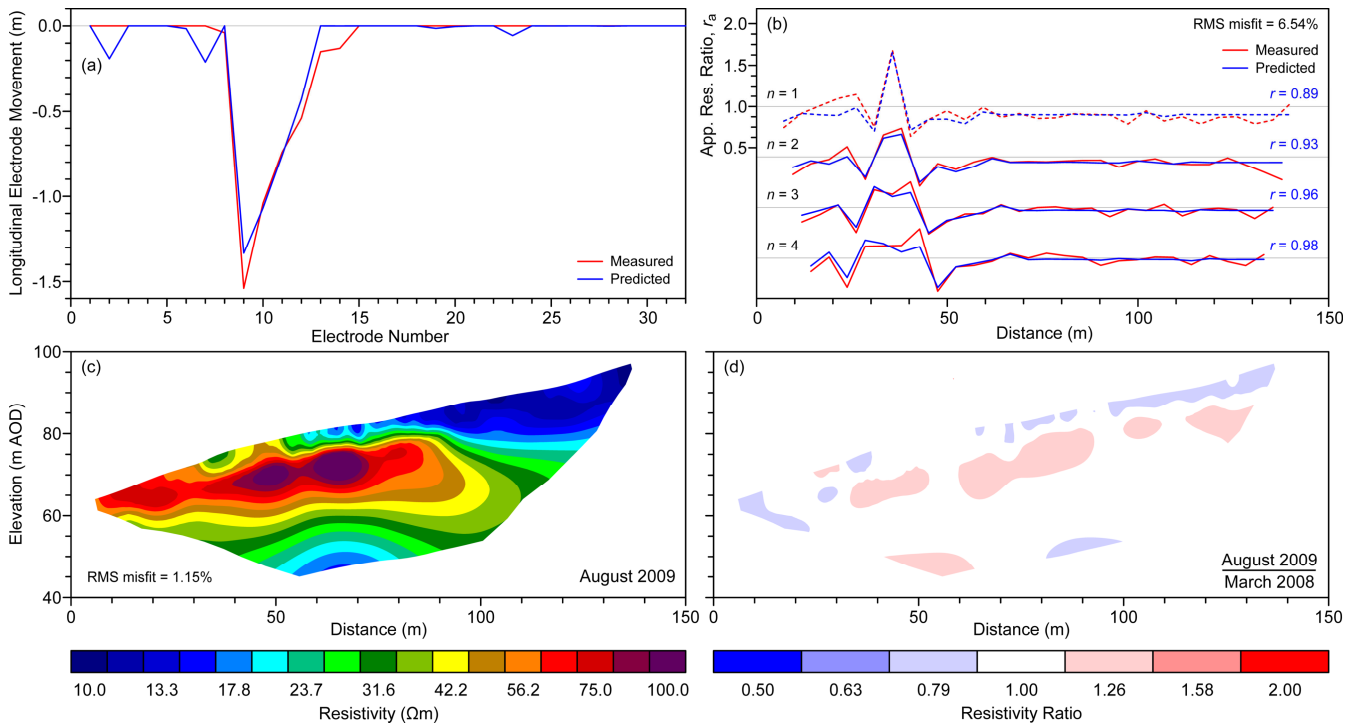


**Figure 10.** August 2009 (a) measured (red) and predicted (blue) longitudinal electrode movements. (b) measured (red) and predicted (blue) apparent resistivity ratios and depth-dependent resistivity ratios  $r$  (Data fitted to  $a = 4.75$  m and  $n = 2 - 4$ . Dashed lines show data not used in fit. For each  $n$ -level the light grey horizontal axis indicates  $r_a = 1$ ). (d) and (e) Resistivity and normalised resistivity images obtained after predicted longitudinal position corrections.

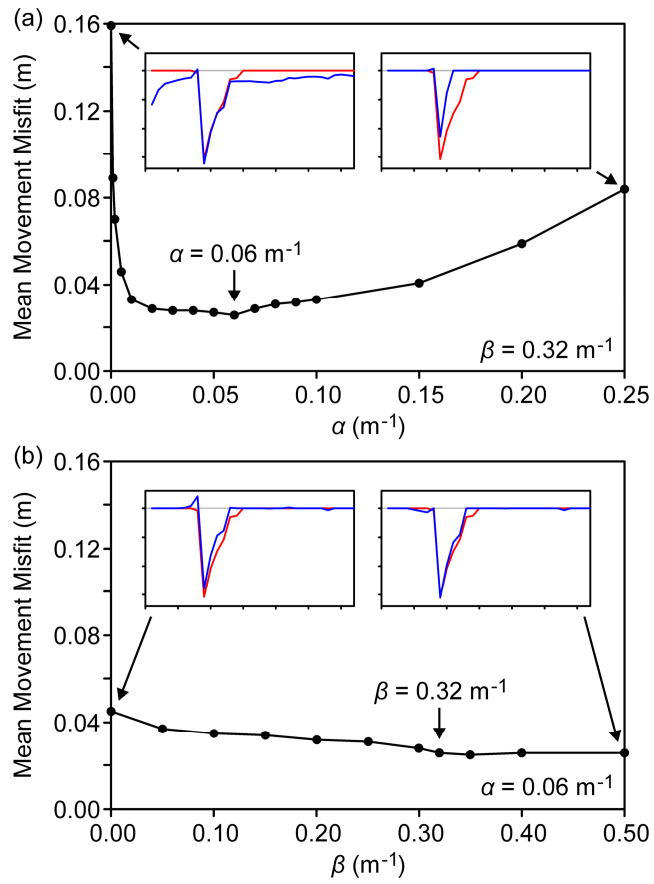


**Figure 11.** Effects of varying (a) the damping constraint and (b) the negativity constraint on the misfit between the inverted and measured electrode movements. Results are for the March 2009 data. Insets show the inverted (blue) and measured (red) movements for the constraint values indicated by the diagonal arrows. The vertical arrows show the constraints used in Figure 9.

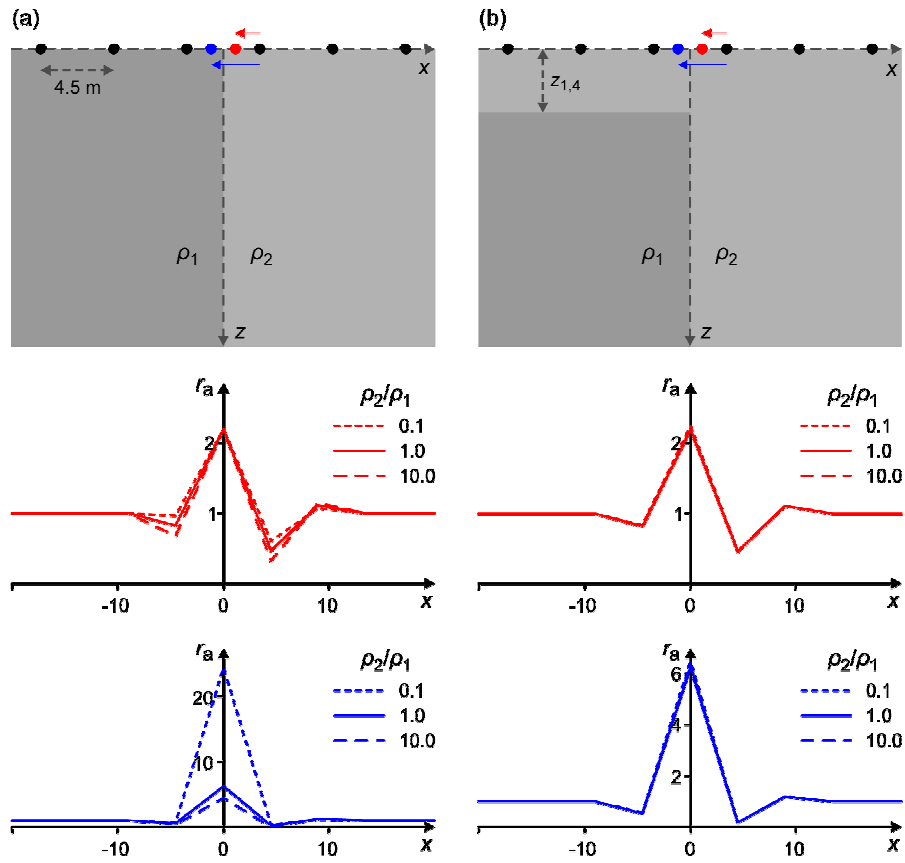


**Figure 12.** Dependence of apparent resistivity ratio  $r_a$  on resistivity contrast  $\rho_2/\rho_1$  in (a) a vertically faulted half-space and (b) a vertically faulted half-space with a covering layer of thickness equal to  $z_{1,4}$  (the median depth-of-investigation of a dipole-dipole configuration with  $a = 4.5$  m,  $n = 4$ ). The red curves show  $r_a$  for  $a = 4.5$  m,  $n = 1$  caused by an electrode displacement that does not cross the fault; the blue curves show  $r_a$  for a displacement that crosses the fault.